Mechanically Compliant and Impedance Matching Hydrogel Bioelectronics for Low-Voltage Peripheral Neuromodulation

*Liangjie Shan, Yu Xue, Xingmei Chen, Yafei Wang, Yinghui Feng, Li Dong, Chang Wang, Pei Zhang, Fucheng Wang, Linna Guo, and Ji Liu**

In neural biointerfacing technologies, mitigating the mismatch in mechanical and impedance attributes between neural tissues and bioelectronics remains a central challenge for achieving high-efficacy neuromodulation. Here, full-hydrogel bioelectronics that demonstrate superior mechanical compliance and impedance matching with 3D peripheral nerves, allowing for low-voltage vagus nerve stimulation, are reported. By precisely tuning the dimensional parameters through 3D printing, the hydrogel bioelectronics, initially in a 2D planar form in a dehydrated state, can curl spontaneously around nerves and form a seamless interface. During the hydration process, instant, and tough bioadhesion is achieved through a dry crosslinking mechanism, enabling a mechanically robust nerve-electrode interface to resist dynamic yet vigorous deformations of the peripheral nerve systems. The as-formed nerve-electrode interface significantly mitigates the impedance mismatch, in favor of electrical stimulation at a threshold voltage of 10 mV, one order of magnitude lower than that of conventional metallic electrodes. The use of the hydrogel bioelectronics for successful stroke rehabilitation through low-voltage vagus nerve stimulation in a rat model is also demonstrated.

1. Introduction

Implantable nerve stimulators provide direct administration of precise electrical stimuli to specific regions, conferring high efficacy in a wide range of neurological disorders, such as Parkinson's disease and epilepsy[1–7] Clinical neural electrodes are generally made of metals, such as gold, in light of their superior conductivity, biocompatibility, structural and electrical robustness.[8,9] However, during long-term implantation, the intrinsic mechanical mismatch leads to severe issues, including nerve compression, inflammatory reactions, and encapsulation by non-conductive fibrous tissue, which progressively impairs stimulation efficacy (**Figure** 1a,b).[4,10–16] Furthermore, the elevated impedance at the electrode-tissue interface necessitates a higher charge density and stimulation voltage, which increases the risk of tissue damage and potentially adverse effects on other physiological functions such as cardiac arrhythmias.[17,18] Consequently, the mechanical and impedance mismatch at the current nerve-electrode biointerfaces poses a significant obstacle to the long-term reliability of implantable neuromodulation devices.

To mitigate these limitations, new electrodes are being developed with sophisticated structural designs, i.e., ultrathin configurations and porous networks. These electrodes could offer mechanical compliance with neural tissue, thereby reducing the risk of mechanical injury.[12,19–21] However, as the implantation of these electrodes often requires intricate surgical procedures to ensure accurate placement and mechanical anchorage onto nerves, the use of sharp surgical tools and fixation with sutures is inevitable.[22] Hence, it is desired that these neural electrodes can be spontaneously and seamlessly wrapped around the 3D surfaces of nerves.[23,24] Recent advancements in smart materials have greatly accelerated the development of self-morphing neural electrodes, which can be triggered by light irradiation,[25] temperature changes,[23] electrochemical drives,[26] or programmed inner stress.[27] Despite these advancements, it may be challenging for neural electrodes with either 3D cuff/spiral or standard 2D planar designs to form effective contacts at the nerve-electrode interface or accommodate nerves of different diameters.[28] Further, the presence of a gap or nerve compression at the nerve-electrode interface could significantly deteriorate the stimulation efficiency.[29] Additionally, physical wrapping often results in inherently weak and fragile nerve-electrode biointerfaces, potentially accompanied by electrode misalignment, dislocation, and even interfacial failure under the dynamic conditions of nerve movement.[30,31]

Herein, we report mechanically compliant and impedance-matching hydrogel-based bioelectronics that undergo self-curling when in contact with wet peripheral nerves and form conformal neural interfaces (Figure 1c). Through 3D multi-material printing, hydrogel bioelectronics were fabricated with tailored geometrical parameters (i.e., overall thickness, thickness ratio, and aspect ratio), imparting them with distinct self-curling characteristics (Figure 1d,e). Before surgical implantation, the

---

L. Shan, Y. Xue, X. Chen, Y. Wang, Y. Feng, L. Dong, C. Wang, P. Zhang, F. Wang, L. Guo, J. Liu
Department of Mechanical and Energy Engineering
Southern University of Science and Technology
Shenzhen 518055, China
E-mail: liuj9@sustech.edu.cn

The ORCID identification number(s) for the author(s) of this article can be found under https://doi.org/10.1002/adma.202511014

DOI: 10.1002/adma.202511014

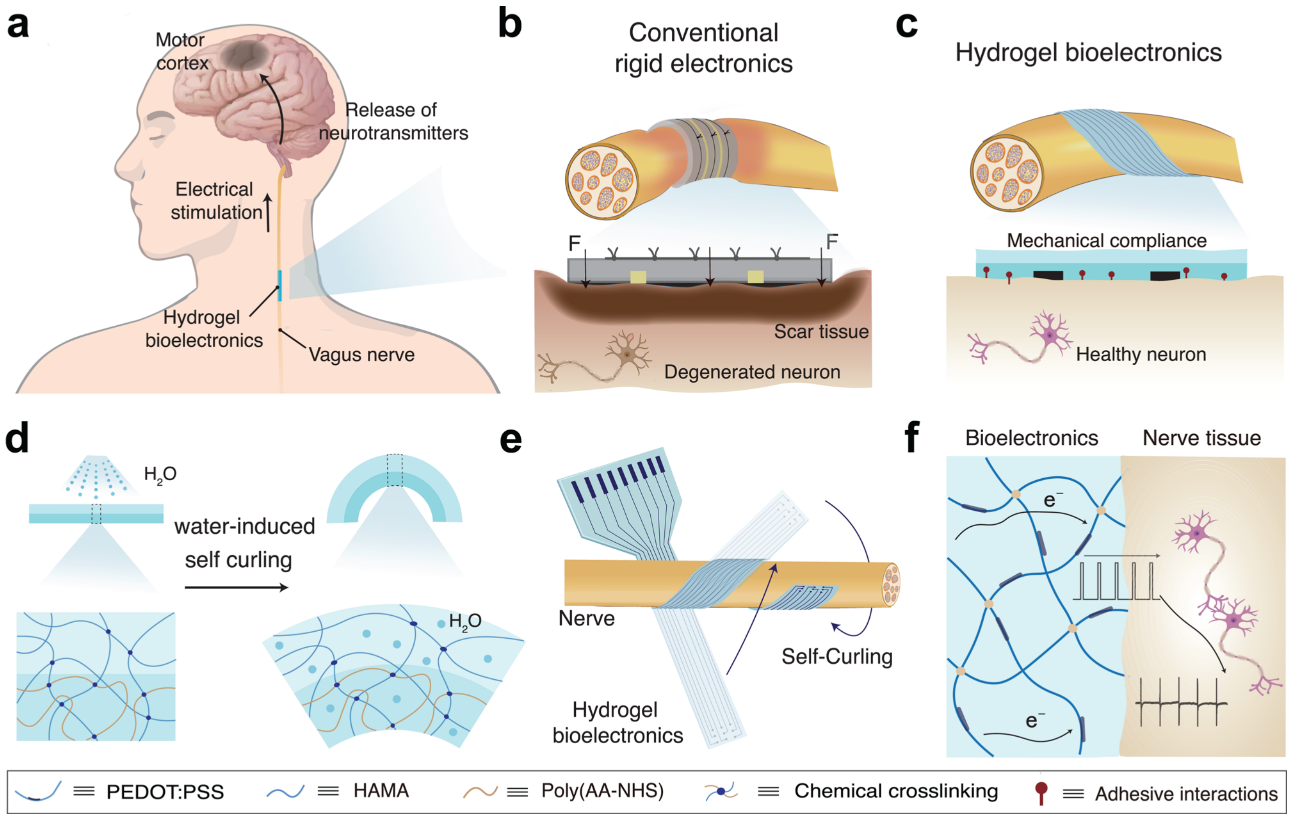

Figure 1. 3D printed hydrogel bioelectronics for neural intervention through electrical stimulation. a) Schematic illustration of stroke rehabilitation through electrical intervention of the vagus nerve system using 3D-printed hydrogel bioelectronics. b) Traditional rigid electrodes (i.e. gold or platinum) are challenged by the mismatch between the mechanical and impedance attributes of neural tissues, leading to low-efficiency electrical biointerfacing. While sutures enable the robust anchorage of rigid electrodes onto neural tissues, mechanical piercing may also induce undesirable inflammatory responses and scar formation, further deteriorating the biointerfacing efficacy. c) Hydrogel-based bioelectronics offer mechanically compliant and impedance-matching biointerfaces, while interfacial bioadhesion enables a conformable interface with peripheral nerves against vigorous and periodic deformation during daily biological functions. d) Structural morphing of an asymmetric polymer film upon hydration in light of non-uniform swelling dynamics, swelling ratio, and mechanical modulus. e) Self-curling of the hydrogel bioelectronics on neural tissues during hydration. f) Schematic of the electrical biointerface between the conducting hydrogel electrode and neural tissues.

hydrogel bioelectronics were temporarily flattened to a 2D planar form in a dehydrated state while naturally self-curling onto the nerves to form 3D flexible neural interfaces. During the hydration process, bioadhesion between the hydrogels and nerve tissues occured through a dry crosslinking mechanism; thus, no additional surgical fixation is required. Accompanied with the dramatic deformations of peripheral nerves, such as bending, twisting, and stretching, these hydrogel bioelectronics could conformally deform with the nerves without interfacial failure. Furthermore, the significantly mitigated impedance mismatch enabled high-efficacy electrical neuromodulation at a much lower threshold stimulation voltage (Figure 1f). Finally, stroke rehabilitation was validated using vagus neural stimulation via the proposed hydrogel bioelectronics.

2. Results and Discussion

2.1. Fabrication of the Hydrogel Bioelectronics

Hydrogel bioelectronics were fabricated using extrusion-based direct ink writing (DIW) 3D printing technology (**Figure** 2a,b; Movie S1, Supporting information). Specifically, hydrogel precursor inks with rheologically tailored performances were pneumatically extruded through a nozzle and then solidified to form 3D structures. The hydrogel inks were formulated of long-chain polymer precursors, including methacrylated hyaluronic acid (HAMA), poly(ethylene glycol) diacrylate (PEGDA, M_w = 2000 Da), with trace-amount of α-ketoglutaric acid as photoinitiator. To impart hydrogel inks with electron conductivity as the conducting layer, poly(3,4-ethylenedioxythiophene): poly(styrenesulfonate) (PEDOT: PSS) was added as a conducting filler in an optimized filling ratio of 6 *wt*%. This ratio was determined by evaluating the printing outcomes under varying parameters, such as applied pressure, nozzle diameter, and ink composition (Figures S1 and S2, Supporting information). To engineer a hydrogel ink with bioadhesion capability, a poly(acrylic acid-*co*-hydroxyethyl methacrylate-*co*-*N*-hydroxysuccinimide ester) (PANH, 15 *wt*%) copolymer was added as the functional moiety, imparting instant and tough bioadhesion to the hydrogel through the dry crosslinking mechanism.[32,33] The distinct shear-thinning and stress-yielding performances ensured smooth extrusion through the nozzle and enabled rapid

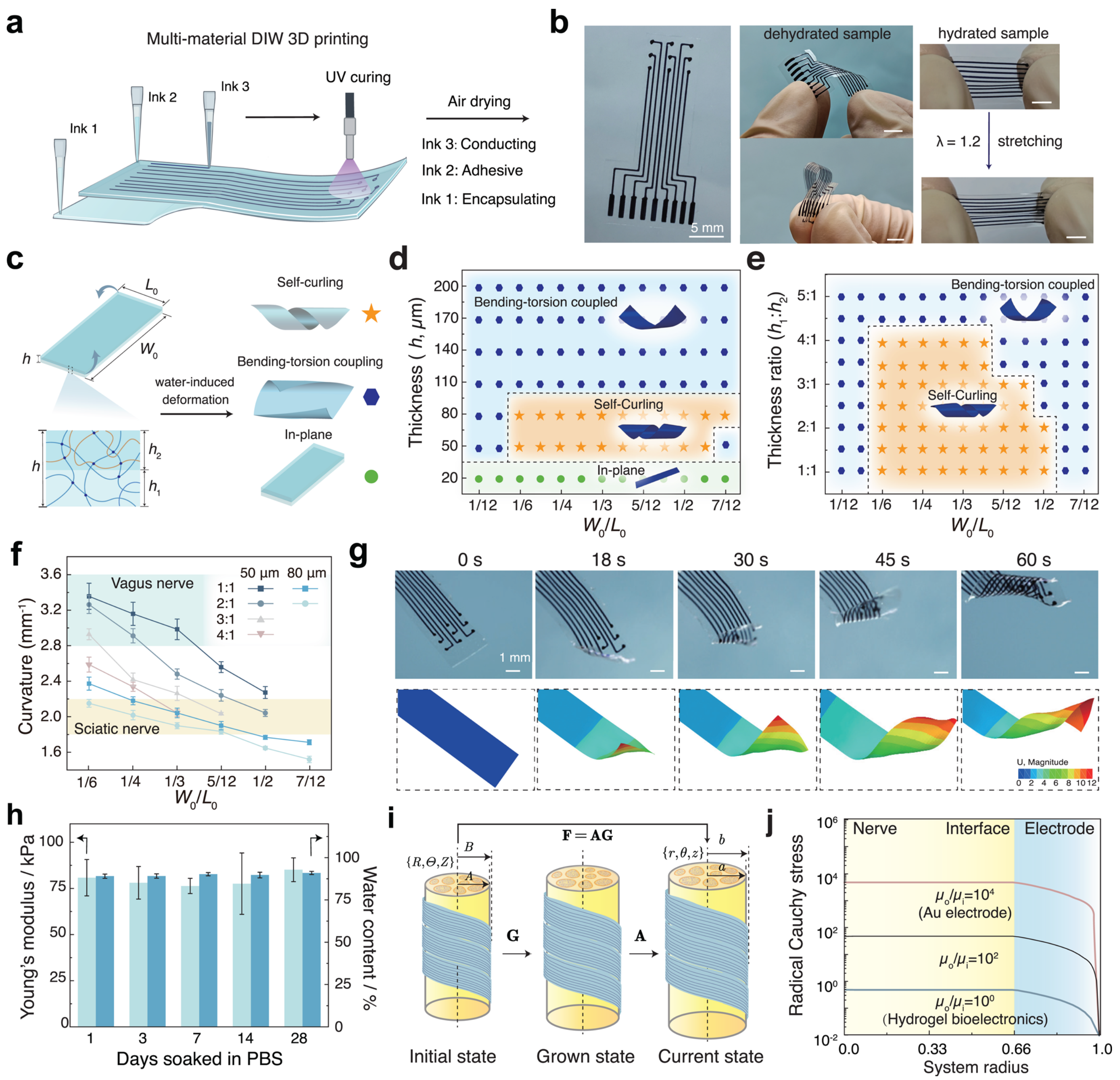

Figure 2. Mechanical compliance of the hydrogel bioelectronics. a) Schematic illustration of 3D printing hydrogel bioelectronics from DIW 3D printing technology. Three different hydrogel precursor inks: the conductive ink, the encapsulation ink, and the bioadhesion inkwere utilized to fabricate the hydrogel bioelectronics through multi-material 3D printing. b) Images of a 9-channel hydrogel bioelectronics. The free-standing and flexible sample could be stretched by 1.2 times without failure upon hydration. Scale bar: 5 mm. c) Deformation modes (self-curling, bending-torsion coupled or in-plane) of the hydrogel bioelectronics could be rationally tailored by optimizing the dimensional parameters, including overall thickness (h), aspect ratio (W_0/L_0) and the thickness ratio (h_1/h_2) d,e) Phase diagram illustrating the reliance of deformation modes on the W_0/L_0 and h, as well as the W_0/L_0 and h_1/h_2 at a fixed overall thickness of 50 µm. The dimensional parameters could be precisely controlled through 3D printing. f) Reliance of curvature on W_0/L_0 and h_1/h_2 for hydrogel bioelectronics with self-curling behaviors.The yellow-shaded area indicates the curvature range of the sciatic nerve, while the blue-shaded area represents the curvature range of the cervical vagus nerve. g) Experimental and FEA simulation of the self-curling process for 3D-printed hydrogel bioelectronics. h) Mechanical and compositional stability of the hydrogel bioelectronics during a 28-day storage in PBS buffer. i) Mechanical model of the 3D-printed hydrogel bioelectronics-nerve interface according to the volumetric growth theory. j) Radial Cauchy stress of the electrode-nerve interface according to various modulus matching coefficients (μ_o/μ_i), where μ_o and μ_i represent the Young's modulus of the electrode and nerve tissue, respectively. Data in (f) and (h) are presented as means ± S.D., n = 3.

solidification, resulting in the formation of high-fidelity filaments (Figures S3– S7, Supporting information).

By utilizing the multi-material DIW 3D printing, fully hydrogel-based bioelectronics could be readily fabricated (Figure 2a). Upon air drying, the dehydrated sample could be stored under –20 °C for over 6 months prior to use (Figure 2b). Owing to the interfacial chain entanglement and the formation of covalent bonds, robust and coherent adhesion was formed at each heterogeneous interface within the hydrogel bioelectronics (Figures S8 and S9, Supporting information). The resulting hydrogel bioelectronics exhibited distinct flexibility in the dehydrated state (Figure 2b). Upon exposure to a wet tissue, the prompt hydration process could drain the interfacial water and facilitate direct contact between the polymer chains and biological tissues, forming a tough biointerface through the synergistic contribution from interfacial chemical anchorage and non-covalent interactions.[32,33] Moreover, the hydrated bioelectronics samples exhibited a modulus of 80 kPa and stretchability of 120%, featuring nerve tissue-like mechanical compliance (Figure S10, Supporting information).

2.2. Tailored Self-Curling Characteristics of the Hydrogel Bioelectronics

Electrical neuromodulation has been widely used as a therapeutic strategy for treating various neural disorders such as epilepsy; however, geometrical mismatches at the electrode-nerve interfaces and complicated electrode implantation can negatively impact efficacy and reliability of neuromodulation.[3,11] Electrodes that exhibit self-curling characteristics when triggered by various stimuli have emerged as alternatives to form conformal neural interfaces.[23,25,26] In contrast to bilayer systems comprising a swelling hydrogel and a passive, non-expanding layer,[34] this study proposes an alternative design in which both hydrogel layers are active and stimuli-responsive. By tuning their chemical composition and crosslinking density, we achieved programmable modulation of the Young's modulus for each layer, thereby establishing a continuous mechanical gradient across the thickness direction(Figure S11, Supporting information). This gradient caused uneven internal stress distribution during the hydration process (Figure S12, Supporting information), inducing varying expansion ratios across different thicknesses and resulting in a strain-stress mismatch. Even when hydrogel films exhibit isotropic swelling in-plane (along the x/y directions), a gradient in crosslinking density across the thickness can lead to non-uniform bending due to swelling mismatch between the top and bottom layers. More importantly, the direction and complexity of the resulting 3D deformation are not solely determined by the swelling mismatch, but are also significantly influenced by the original planar geometry of the hydrogel, such as the aspect ratio (W_0/L_0) ratio and total thickness (h).[34] A bimetallic strip model can well describe this deformation mechanism.

$$M = \frac{EI}{\rho} \propto k \cdot \Delta l \cdot h^2 \tag{1}$$

Where EI is the bending rigidity of a hydrogel layer, and ρ is the radius of the bending curvature. The M is positively related to the length difference before and after swelling of one side (Δl) and square to the thickness of the hydrogel film (h), and k is a Young's modulus-related parameter. The internal bending moments along the x- and y-axes (M_x and M_y) are modulated by these geometric parameters, collectively giving rise to the resultant bending moment M_{xy}.[35] In this model, the coupling between internal stress distribution and structural geometry governs the final deformation path. Previous studies have shown that by tuning W_0/L_0 or h, the relative magnitude of M_x and M_x can be adjusted, enabling the hydrogel structure to evolve along asymmetric or helical deformation pathways, in accordance with the principle of energy minimization.[36,37] Specifically, when the device exhibits a symmetric geometry, the self-curling behavior typically occurs along the edge direction, resulting in a relatively regular rolling or tubular configuration (Figure 2c). This behavior primarily arises from the isotropic distribution of internal stress, while in the absence of a dominant geometric axis, the system tends to curl uniformly along each dimension. With the aspect ratio increased (i.e., >1), the geometric constraints along the length and width directions become asymmetric, inducing anisotropic stress distribution within the bilayer structure, thus it preferentially adopts a helical or spiral curling morphology to minimize its total elastic energy.

We then employed finite element analysis (FEA) to explore the different deformation modes of the hydrogel bioelectronics during the hydration process, including self-curling, bending-torsion coupling, and in-plane deformation (Figure 2c, Supporting information).[38] Using 3D printing technology, the aspect ratio W_0/L_0 and thickness (h) of the bioelectronics could be precisely controlled (Figure 2d). Additionally, by adjusting the thickness ratio of the two layers (h_1/h_2; Figure 2e; Figure S13, Supporting information), the deformation modes of bioelectronics under different conditions were determined. Compared to conventional fabrication methods, DIW enables more rapid and programmable construction of complex, multi-material bioelectronic architectures (Table S1, Supporting information). To validate the design rationale of swelling-induced deformation, we fabricated hydrogel samples with identical aspect ratios but different thicknesses through 3D printing. Upon hydration, these samples exhibited distinct deformation modes, including in-plane expansion, bending-torsion coupling, and self-curling, highlighting the critical role of geometric parameters in shaping 3D transformation (Figure S14, Supporting information). Subsequently, specific dimensional parameters for achieving the self-curling deformation mode were selected, and FEA was used to evaluate the effect of each parameter on the curvature. The results can serve as a guide for the customized fabrication of hydrogel bioelectronics that could be tailored for biological tissues with varying curvatures (Figure 2f). The self-curling capability enables hydrogel bioelectronics to autonomously transition from a 2D planar state to a 3D structure, thereby adapting to complex geometries to achieve optimal shape conformity with biological tissues, particularly in applications involving tubular structures such as nerves. Guided by Figure 2f, we customized the dimensional parameters of hydrogel bioelectronics for the sciatic nerve (curvature of ≈2 mm^{-1}): h of 80 µm, h_1/h_2 of 1:1, and W_0/L_0 of 1/3. Upon direct contact with water, the hydrogel bioelectronics rapidly self-curled (within 60 s), which was in good agreement with the FEA simulation under the same conditions (Figure 2g; Figure S15 and Movie S2, Supporting information).

Although the hydrogel bioelectronics with self-curling capability can effectively form a mechanically conformable neural-electrode biointerface, dislocation may happen during the peripheral movement.[30,31] To improve interfacial anchorage, we engineered the hydrogel bioelectronic with superior bioadhesion performance through the dry-crosslinking mechanism. It involves immediate drainage of interfacial water through dehydration of the polymer films, followed by the formation of covalent and non-covalent interactions at the interface (Figure 1), resulting in robust biointerface with the tissues. Specifically, covalent bonds are formed through reactions between NHS ester groups and amine groups on the tissue surface, accompanied by non-covalent interactions such as hydrogen bonding.[32,33] The adhered joints exhibited high shear strength (120 kPa) and interfacial toughness (200 $\mathrm{J\,m^{-2}}$, Figure S16, Supporting information).

Moreover, after soaking in phosphate-buffered saline (PBS) buffer for 14 days, the adhesion joints maintained a desirable mechanical integrity. Such instant and tough bioadhesion allows for mechanically robust biointerfaces with small-diameter tubular tissues such as nerve tissues.

2.3. Mechanical Compliance of the Hydrogel Bioelectronics

The fully swollen hydrogel bioelectronics exhibited a high water content of 90% and Young's modulus of 80 kPa (Figure 2h; Figure S10, Supporting Information) despite long-term soaking in PBS buffer, which is comparable to soft tissues, such as nerves, with a Young's modulus in the range of 10–100 kPa.[12] This modulus is significantly lower than that of traditional rigid materials used in bioelectronics, such as gold (3.5 GPa). Meanwhile, we quantitatively characterized the bending stiffness of both the hydrogel bioelectronics and the Au electrode, revealing that their bending stiffness was two orders of magnitude lower (Figure S17, Supporting Information). Together, these findings demonstrate the formation of a mechanically compliant biointerface. To better understand the mechanical compliance of the neural electrode interface, we developed a mechanical model based on the volumetric growth theory (Figure 2i).[41] In this model, the initial radius of the neural tissue is assumed to be A, and the thickness of the electrode system is represented as $(B-A)$. Growth (active tensor G) is introduced, allowing the system to transition from its initial state to its growth state. The growth state was a virtual and discrete state, whereas a pure elastic tensor A was required to ensure geometric compatibility, transitioning the system from the growth state to the current state. In the current state, the radius of the nerve is a and the electrode thickness is $(b-a)$. From the initial state to the current state, the overall deformation gradient tensor $\mathbf{F}$ is generated as follows:

$$\mathbf{F} = \mathbf{A}\,\mathbf{G} \tag{2}$$

Furthermore, the constitutive model (incompressible) for the neural tissue-hydrogel electrode system can be described using the following relation:

$$\Psi = \frac{\mu}{2}\left(\mathbf{C}_a : \mathbf{I} - 3\right) \tag{3}$$

where Ψ is the strain energy density, μ is the shear modulus of the material, $\mathbf{C}_a = \mathbf{A}^{\top}\mathbf{A}$ is the right Cauchy-Green deformation tensor, and $\mathbf{I}$ is the identity tensor. Based on this strain energy density function, the Cauchy stress tensor T can be derived as follows:

$$\mathbf{T} = \mathbf{A}\frac{\partial \Psi}{\partial \mathbf{A}} - q\mathbf{I} = \mu\mathbf{A}\mathbf{A}^{\top} - q\mathbf{I} \tag{4}$$

where q is a Lagrange multiplier used to enforce incompreesibility. Considering the first Cauchy equation, div $\mathbf{T} = 0$, we obtained the expression for the radial Cauchy stress, as shown in Figure 2j. The radial Cauchy stress induced by the hydrogel bioelectronic was four orders of magnitude lower than that induced by the Au electrode. To enhance clarity and reproducibility, a full derivation of the radial Cauchy stress and the definitions of all involved variables are provided in the Supplementary Information. Similarly, FEA results confirmed that the pressure exerted on the neural tissue by the hydrogel bioelectronics was approximately two orders of magnitude lower than that of Au electrodes (Figure S18, Supporting information). This corroborates the distinct advantage of our hydrogel bioelectronics in terms of a mechanical modulus matching that of neural systems. We wrapped the hydrogel bioelectronics around the sciatic nerve of a free-moving rat for 4 weeks. Simultaneously, a cuff electrode made of polyethylene terephthalate (PET) and an Au thin film (thickness of 80 μm) was implanted for comparison. Hematoxylin and Eosin (H&E) staining and CD68 immunofluorescence staining of the nerve bundles revealed that the inflammatory response induced by our hydrogel bioelectronics (0.52 ± 0.17) was ≈20 times lower than that of PET-Au electrode (11.62 ± 3.7) (Figure S19, Supporting information).

2.4. Impedance Matching of the Hydrogel Bioelectronics

PEDOT: PSS is a typical conducting polymer with water-rich properties that enable rapid ion penetration into the polymer network. The polymer backbone forms a nanometer-scale electric double layer (EDL) with a high volumetric capacitance, unlike the areal capacitance of traditional metallic electrodes (**Figure 3a**).[9,42] It significantly mitigates the interfacial impedance of biological tissues/organs, thus enhancing high-efficacy bioelectronic recordings and low-voltage stimulation. Enhanced phase separation between PEDOT and PSS, induced by *N*-methacryloyl glycine (MAG), resulted in hydrogels with significantly improved conductivities and stability, i.e., 6 $\mathrm{S\,cm^{-1}}$ over 28-day soaking in PBS buffer (Figure S20, Supporting Information). The long-term stability of the charge storage capacity (CSC) and voltage-pulse charge injection capacity (VPCIC) in the range of –0.5–0.5 V was corroborated by the slight change in CSC (<5%, Figure 3b and Figure S21, Supporting Information) after 1000-cycle CV scanning, and VPCIC (<10%, Figure 3c; Figure S21, Supporting information) after 100 000-cycle biphasic charge injection into PBS buffer. Such superior charge storage and injection capabilities are crucial for effective and reliable electrical stimulation of the neural systems. Additionally, the conductivity of the adhesion and encapsulation layer was 0.0006 and 0.005 $\mathrm{S\,cm^{-1}}$ (Figure S22, Supporting information), respectively, which could ensure efficient insulation during the electrical stimulation. It is worth noting that 1 kHz has emerged as a commonly accepted reference frequency for characterizing implantable

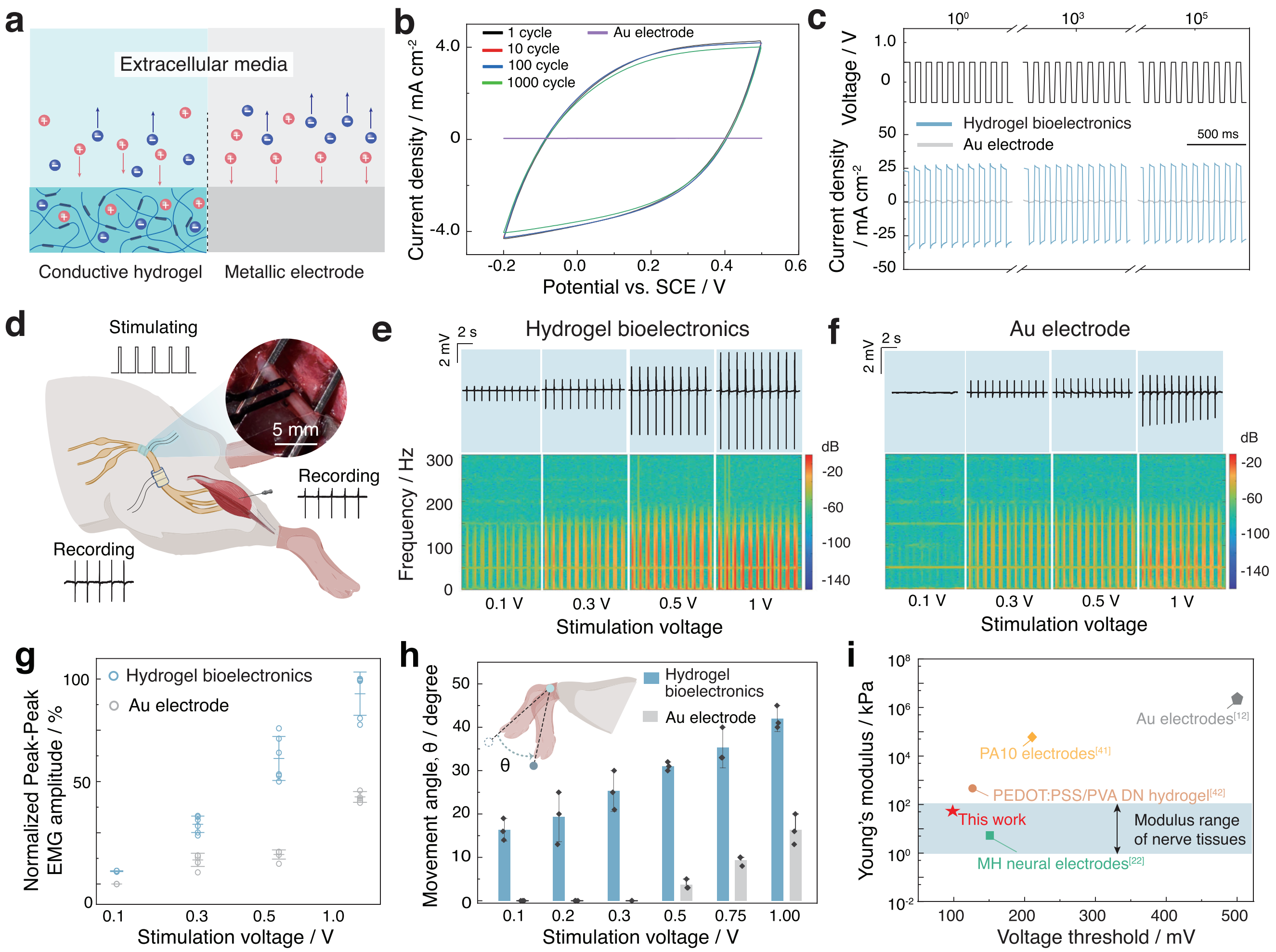

Figure 3. Impedance matching of the hydrogel bioelectronics. a) Capacitive charge injection through a conducting hydrogel electrode and Faradaic charge injection through metallic electrodes. b) Representative cyclic voltammetry (CV) curves of the hydrogel electronics and Au electrodes during the 1000 charge/discharge cycles in PBS buffer. c) Biphasic input pulses (top) and plotting of the corresponding current density versus time (bottom) for the hydrogel bioelectronics and Au electrode at the 1st, 1000th, and 100 000th cycle. d) Schematic illustration and real image of anchoring a 3D-printed hydrogel bioelectronics onto the sciatic nerve for electrical stimulation. e–g) Recorded EMG spectrogram evoked at various voltages (0.1, 0.3, 0.5, and 1.0 V) through the hydrogel bioelectronics (e) and Au electrode (f), as well as plotting of the EMG amplitudes versus stimulation voltages (g). h) Movement angle of the ankle joints triggered through hydrogel bioelectronics and Au electrode at different stimulation voltages. i) Comparison chart of plotting Young's modulus against the voltage threshold to trigger ankle joint movement for various electrodes. Date of other electrodes (Polyamide 10 (PA 10) electrode,[39] PEDOT:PSS/PVA double network (DN) hydrogel,[40] and multifunctional hydrogel (MH) neural electrodes.[22]) were compiled from literatures. Current density data in (b) and (c) are normalized by the surface area of the hydrogel electrodes. Data in (g) and (h) are presented as means ± S.D., $n = 3$ for (b) and (h), while $n = 5$ for (g).

neural interfaces and electrodes. This frequency aligns well with the dominant bandwidth of physiological signals, effectively reflects the typical electrochemical behavior at the electrode-tissue interface in the mid-frequency range, and is sensitive to the frequency-dependent response of different electrode materials. The electrochemical impedance of the hydrogel bioelectronics at 1 kHz remains ≈150 Ω, respectively, even after 28-day soaking in PBS buffer at 37 °C (Figure S23, Supporting information). This stability is comparable to that of previously reported conducting polymer hydrogel systems,[5,9,12,14,20,21,26,27,29] ensuring long-term robust in vivo electrical stimulation (Figure S24, Supporting information).

In vitro cell culture tests confirmed the superior cytocompatibility of our hydrogel bioelectronics through a CCK-8 kit (Figure S25, Supporting information), and live/dead staining analysis (Figure S26, Supporting information). Our hydrogel bioelectronics were fabricated from biodegradable polymers that could be decomposed into biologically benign end products in biological fluids, thus eliminating the need for additional surgical removal. By subcutaneously implanting the hydrogel bioelectronics in a rat model for eight weeks, we clearly observed significant fragmentation and degradation through histological analysis (Figure S27, Supporting information). The complete degradation of these hydrogel bioelectronic samples is expected to occur within a few weeks. Liver and kidney functions after 8-week implantation were comparable to those in the healthy state, indicating no apparent signs of systemic toxicity (Figures S28 and S29, Supporting information).

To probe the low-voltage stimulation efficiency, the terminal region of the conductive hydrogel electrode was directly adhered to the exposed electrode area of a commercial flexible printed circuit (FPC) cable to enable stable external power delivery (Figure S30, Supporting Information). We stimulated the sciatic nerve with our hydrogel bioelectronics as the electrodes and recorded the corresponding electromyographic signal (EMG) and neural electrical signal (NES), while traditional rigid electrodes (i.e., Au electrodes) were used as a control (Figure 3d). With the increase in stimulation voltage from 0.1 to 1 V, the peak-to-peak amplitude of EMG in the hydrogel bioelectronics group gradually increased from 0.5 to 8.5 mV before reaching the saturated value (Figure 3e), in sharp contrast to the moderate change (from 0 to 3.5 mV) for Au electrode (Figure 3f,g). The threshold stimulation voltage, representing the minimum electrical stimulus required to evoke an action potential in muscle tissue, was quantified as 10 mV for the hydrogel bioelectronics. This value is at least one order of magnitude lower than that of Au electrodes (>100 mV, Figure 3f; Figure S31, Supporting Information); this is attributed to the significantly improved impedance matching and conductivity of the hydrogel bioelectronics. A similar difference was observed during NES signal recording upon electrical stimulation, corroborating the role of impedance matching in decreasing stimulation voltages (Figures S32 and S33, Supporting information). Additionally, low-voltage stimulation was validated by electrical stimulation of the sciatic nerves, and the voltage threshold of 100 mV for macroscopic ankle joint movement was much lower than that of the Au electrode (500 mV, Figure 3h; Movie S3, Supporting information). Even though macroscopic limb movement may not provide precise quantification of neuromuscular activation, it is still one of the most widely adopted strategies to preliminarily validate the effectiveness of peripheral nerve stimulation, particularly in sciatic nerve interface studies.[9,12,14,15] Together with the quantitative measurements of both muscle and neural electrical signals (Figure 3e,f), we could conclude that by engineering the hydrogel electrodes with highly desirable impedance-matching properties, low-voltage electrical stimulation could be readily achieved. In addition to their utility as electrodes to deliver electricity for electrical stimulation, hydrogel bioelectronics can also be used as electrodes for electrophysiological signal recording. For example, by gently pinching the rat paw to activate the mechanoreceptor-nerve pathway, our hydrogel bioelectronics recorded the EMG signal with a signal-to-noise ratio (SNR) of 4.5, which was significantly higher than that achieved with the Au electrodes (SNR of 1.7, Figure S34, Supporting information). Such low-voltage stimulation and high-precision electrophysiological signal recording using our hydrogel bioelectronics could significantly improve the efficacy of neuromodulation.

To further demonstrate the mechanical compliance and impedance matching of our hydrogel bioelectronics, we compared them to previously reported electrodes of comparable dimension (≈500 µm in diameter) for neural electrical stimulation (Figure 3i).

Our hydrogel bioelectronics exhibit a Young's modulus within the range of neural tissue (10–100 kPa), which is more than five orders of magnitude lower than that of traditional implantable electrodes such as Au electrodes.[12] Additionally, our hydrogel bioelectronics exhibited a lower voltage threshold (100 mV) for inducing ankle joint movement than nerve stimulation electrodes such as the polyamide 10 electrode,[39] PEDOT:PSS/PVA DN hydrogel,[40] and MH neural electrodes.[22] These characteristics highlight the mechanical compatibility of the hydrogel bioelectronics with neural tissue and their superior electrical stimulation efficiency, making them an ideal tool for clinical neuromodulation and neuroscience research.

2.5. In Vivo Electrical Stimulation over Vagus Nerves

To evaluate the applicability and generality of our hydrogel bioelectronics for low-voltage stimulation, we tested electrical stimulation of peripheral systems, such as the vagus nerve. By tailoring the sample dimension parameters, such as h of 50 µm, h_1/h_2 of 1:1, and W_0/L_0 of 1/6, we could readily 3D print hydrogel bioelectronics with a curvature of ≈3.3 mm^{-1} (Figure 2f), which is specifically used for vagus nerves (diameter of 600 µm). We implanted hydrogel bioelectronics at the vagus nerve site in a rat model, recording NER signals that increased from 0.6 to 10 mV before saturating as the stimulation voltage was increased from 0.01 to 0.5 V. In sharp contrast, the amplitude moderately increased from 0.16 to 4.7 mV (Figures S35 and S36, Supporting information) for the Au electrode group, similar to sciatic nerve stimulation (Figure S32, Supporting information). Since the vagus nerve directly regulates cardiac function, an overdose of electrical stimulation may induce side effects such as arrhythmia or tachycardia (Figure 4a).[17,43] We monitored the electrocardiogram (ECG) signals during stimulation (blue area) to assess the biosafety of vagus nerve stimulation (VNS). With increasing stimulation current, the heart rate continuously increased, returning to normal rate once the stimulation was removed (**Figure** 4b,c; Figures S37 and S38, Supporting information). No side effect on heart rates was evidenced at a stimulation current of 0.25 or 0.5 mA (Figure S39 and Movie S4, Supporting information). Unless otherwise specified, the VNS test used a safe stimulation current of 0.5 mA.

VNS can influence multiple brain regions, including the primary motor cortex (M1), which is responsible for somatic tissue and motor control.[44] Local field potentials (LFPs) represent extracellular potentials surrounding neurons and reflect neuronal activity in the deep brain. After electrical stimulation (0.5 mA, 30 Hz) was applied to the vagus nerve of the rat model, a prompt response in the LFP signals in the M1 region was observed (Figure 4d-e). In neuroscience studies, low-frequency oscillations (LFOs) in the motor cortex have been shown to encode rich information about movement direction, speed, trajectory, and grip type, making them typical targets for stimulation. These oscillations are manifested as transient activity in the motor cortex's δ and θ bands before, during, and after movement initiation.[45] Quantitative analysis of the power spectral density (PSD) of different LFP bands revealed a significant increase in the PSD of LFOs upon stimulation (Figure 4f), the same for other frequency bands (Figure 4g–i). These results indicate that electrical stimulation can significantly modulate neuronal activity in the M1 region, suggesting potential applications of hydrogel bioelectronics in VNS, neuromodulation, and the treatment of neurological disorders.

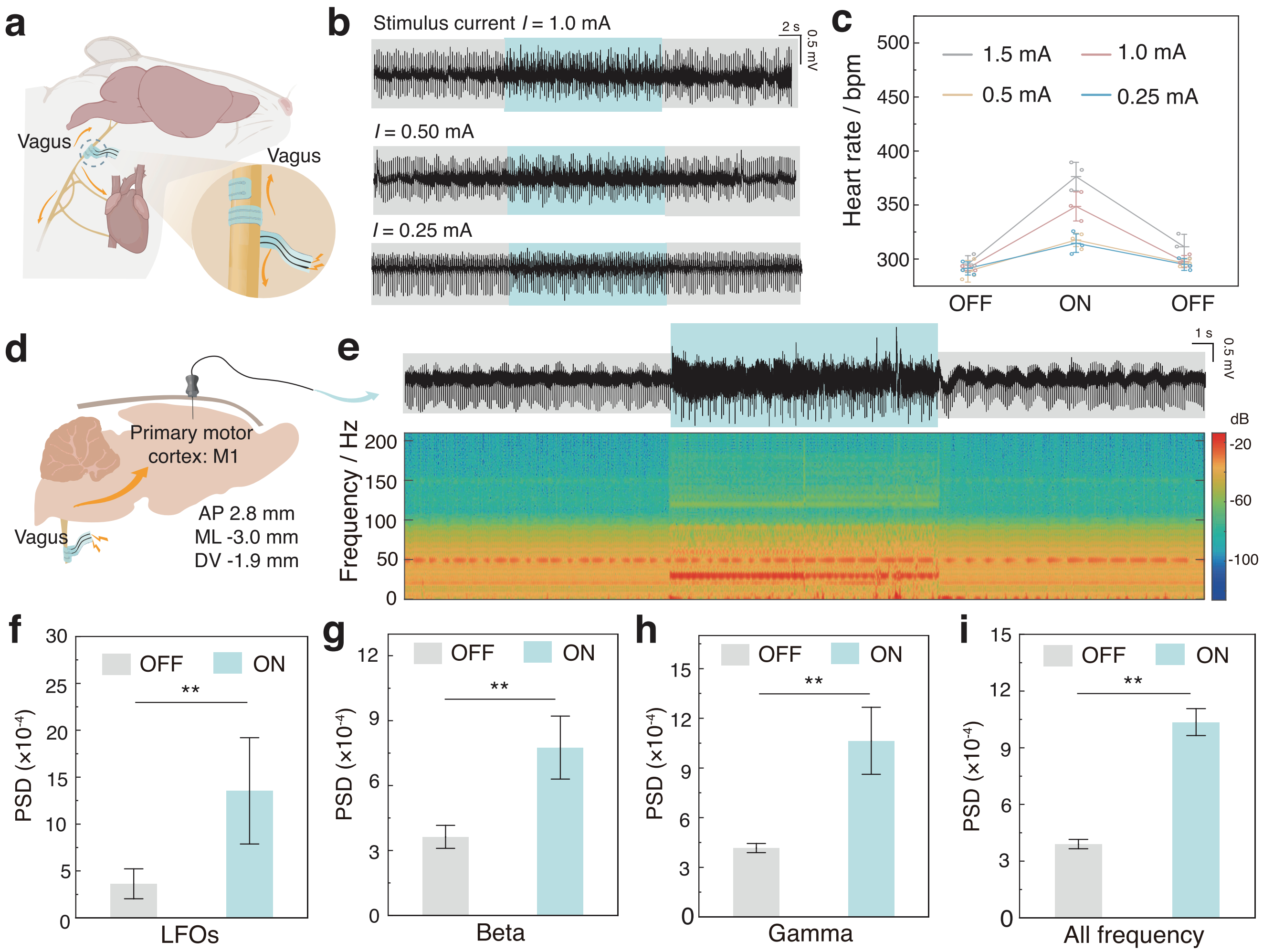

Figure 4. Biosafety and efficacy of hydrogel bioelectronics for vagus nerve stimulation. a) Schematic illustration of implanting a hydrogel bioelectronics sample onto the vagus nerve for electrical intervention in a rat model. b,c) Representative electrocardiogram (ECG) signals recorded at varying stimulation currents (1.0, 0.5, and 0.25 mA) during vagus nerve stimulation (b), and evaluation of heart rate upon vagus nerve stimulation (c). d) Schematic illustration of local field potentials (LFPs) recording in the primary motor cortex (M1) during vagus nerve stimulation. e) LFP signal and corresponding time-frequency analysis during vagus nerve stimulation. f–i) Power spectral density (PSD) analysis of low-frequency oscillations (LFOs, 1–12 Hz, f) beta wave (12–30 Hz, g), gamma wave (30–80 Hz, h), and all frequency wave (1–80 Hz, i) in the motor cortex before (OFF) and after (ON) vagus nerve stimulation. Data are presented as means ± S.D., ($n = 5$). Statistical significance and p values were determined by the ANOVA-test method; ns, not significant; $^{*}p < 0.05$, $^{**}p < 0.01$, $^{***}p < 0.001$.

2.6. Rehabilitation of Limb Motor Function

Stroke is one of the most common diseases that frequently causes motor dysfunction, a prevalent complication that severely affects patients' quality of life. Recently, VNS has emerged as a promising therapy for neurorehabilitation because of its effectiveness in inducing the precise temporal modulation of neurons in response to behavioral outcomes, which can help restore motor function in hemiplegic limbs.[6,46–48] Subsequently, we applied our hydrogel bioelectrodes to low-current VNS to investigate their potential application in accelerating stroke recovery and promoting motor function restoration. Rat models with ischemic stroke were established through endothelin-1 injection following previously reported protocols.[46,49] The experimental procedures are outlined in **Figure** 5a. Endothelin-1 induced local vasoconstriction and reduced blood flow into brain tissues, thus causing ischemic stroke. Changes in cerebral blood flow (CBF) at various stages were monitored using laser speckle contrast imaging (LSCI) (Figure 5b). Upon endothelin-1 injection, a rapid decrease in CBF was observed in the stroke model. Electrical intervention through VNS (referred to as Stim(+)) resulted in significant recovery of blood flow during the 1- and 2-week treatments, while the stroke groups without VNS treatment (referred to as Stim(−)) showed negligible changes within 2 weeks. The therapeutic effect of VNS is attributed to its ability to upregulate the expression of angiogenic biomarkers, thereby accelerating vascular regeneration and blood flow restoration.[50] The brain tissue sections were analyzed using 2,3,5-triphenyl tetrazolium chloride (TTC) staining (red for healthy brain tissue, white for infarcted tissue) to quantify the infarct volume of 9.0 ± 2.2% after 2-week VNS treatment, which was significantly smaller than the Stim (−) group (20.0 ± 2.8%, Figure 5c; Figure S40, Supporting information).

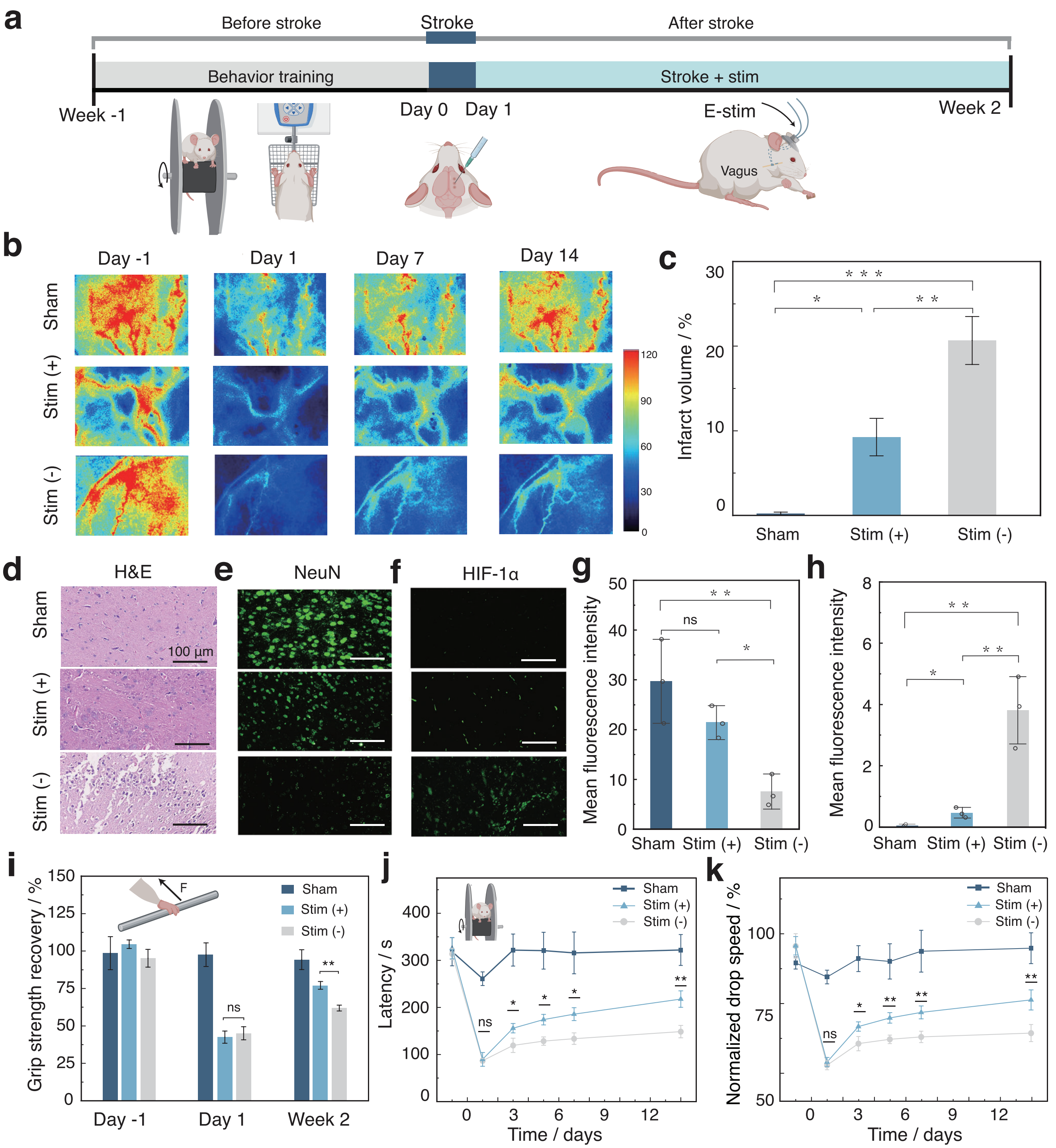

Figure 5. Hydrogel bioelectronics-based neuromodulation for stroke rehabilitation. a) Experimental design and timeline for stroke rehabilitation through electrical neuromodulation. b) Representative LSCI images for cortical blood flow during the stroke management through VNS. c) Quantitative infarct volume upon 2-week rehabilitation for different groups, including the stroke with VNS treatment (Stim (+)), stroke without VNS treatment (Stim (−)), and the normal control group (Sham). d–f) Histological analysis through H&E (d), and immunofluorescence imaging of the brain tissues stained with neuronal nuclear marker protein (NeuN) antibody (e) or hypoxia-inducible factor-1α(HIF-1α) antibody (f). g,h) Average fluorescence intensity of NeuN (g) or HIF-1α staining (h) for different groups. i–k) Behavior evaluation based on the forelimb gripping and rotating beam tests, and quantitative evaluation of forelimb grip strength recovery (g), latency (h), and normalized drop speed (i) during the 2-week rehabilitation for different groups. Data in (c), (g–k) are presented as means ± S.D., $n = 3$. Statistical significance and p values were determined by the ANOVA-test method; ns, not significant; $^{*}p < 0.05$, $^{**}p < 0.01$, $^{**}{}^{*}p < 0.001$.

H&E staining revealed that compared to the Stim (−) group, the Stim (+) group of stroke rats exhibited significantly reduced neuronal necrosis and apoptosis in the infarct area (Figure 5d). NeuN, a neuron-specific nuclear protein, is not expressed in the infarcted region, and therefore is used as a biomarker to identify damaged neurons. After 14 days of VNS treatment, NeuN levels in the infarcted area of stroke rats significantly increased. Specifically, the NeuN fluorescence intensity in the infarcted region of the Stim (+) group (21.47 ± 3.25) was 3-fold that of the Stim (−) group (7.55 ± 3.17). Moreover, stroke-induced local ischemia and hypoxia led to a significant reduction in the infarction tissue marker hypoxia-inducible factor 1 alpha (HIF-1α) upon Stim (+) treatment, decreasing by 8.3-fold (0.46 ± 0.16) compared to the Stim (−) group (3.8 ± 1.2) (Figure 5f,h). These results corroborate the role of VNS delivered through hydrogel bioelectronics at low current levels in reducing the infarct size and promoting stroke recovery.

Strokes often result in hemiplegia or motor dysfunction. To evaluate the effects of VNS on motor function recovery in the stroke rats, grip strength and rotarod tests were used to quantitatively assess motor coordination and balance.[6] Parameters were measured on Day -1 (pre-stroke) and days 1, 3, 5, 7, and 14 (post-stroke). As illustrated in Figure 5i, after 14-day VNS treatment, the forelimb grip strength in the Stim (+) group recovered to 74.4 ± 3.6% of the pre-stroke level. In contrast, grip strength in the Stim (−) group only reached 58.3 ± 2.9%. Various parameters were evaluated using the rotarod test, including traversal time, falling speed, and traversal duration across different groups. The Stim (+) group experienced significant improvements in these parameters, compared to the Stim (−) group (Figure 5i–k; Figures S41 and S42 and Movie S5, Supporting information). Notably, introducing VNS shortly after stroke led to remarkable short-term enhancements in forelimb motor performance in stroke rats and sustained superior motor outcomes throughout the extended treatment period. These findings confirm that hydrogel bioelectrodes for VNS can significantly accelerate stroke recovery and restore motor function.

3. Conclusion

In summary, we report the customized fabrication of 3D-printed hydrogel bioelectronics, which were tailored to peripheral nerves of varying curvatures by examining the influence of geometric parameters, including total thickness, thickness ratio, and aspect ratio, on the self-curling behavior of bioelectronics. Coupled with the bioadhesion capability enabled by a dry crosslinking mechanism, hydrogel bioelectronics naturally adapt to nerve deformation without inducing persistent damage, thus forming a seamless and robust nerve-electrode biointerface. Moreover, the significantly reduced impedance mismatch facilitated efficient electrical neuromodulation at a much lower threshold stimulation voltage (10 mV). The proposed hydrogel bioelectronics were applied in a rat stroke model to successfully demonstrate that low-current stimulation of the vagus nerve can accelerate stroke recovery and promote motor function restoration. This study represents a significant advancement in neural electrode design, universal neural interfacing, and neuromodulation, and provides a critical tool for understanding neural information and addressing brain dysfunction.

4. Experimental Section

4.0.0.1. Synthesis of the PAHN Copolymer: The poly(acrylic acid-co-hydroxyethyl methacrylate-co-*N*-hydroxysuccinimide ester) (PAHN) copolymer was synthesized as follows: 9.5 g AA (130 mmol), 0.67 g AA-NHS ester (3.95 mmol), and 0.356 g HEMA (2.67 mmol) were dissolved in dry and degassed DMSO, together with 0.020 g (0.12 mmol) AIBN as initiator, followed by polymerization at 70 °C for 8 h. Subsequently, the reaction was cooled down to room temperature to halt the polymerization. A solution containing 3 mmol of IEA and 0.08 µmol of dibutyltin dilaurate in DMSO (10 mL) was slowly fed into the reactant under vigorous stirring within 5 min, and the mixture was allowed to react overnight at room temperature. The resulting crude product was precipitated three times into excessive acetone, and then vacuum-dried at room temperature to yield the pure product (yield of ≈80%).

4.0.0.2. Synthesis of Methacrylated Hyaluronic Acid (HAMA): In brief, 2.5 g hyaluronic acid (M_w = 20–40 kDa) was dissolved in 125 mL of Milli-Q water in a three-neck round-bottom flask under vigorous stirring at room temperature until complete dissolution. The mixture was then cooled down with an ice bath, and the pH of the mixture was adjusted to 8.5 by dropwise adding 1.0 mol L^{-1} NaOH. 5.625 mL of methacrylic anhydride (MA, 38 mmol) was dropwisely added. The reaction was performed for 4 h at 0 °C, while the pH was maintained in the range of 7.5–8.5. After that, the solution was vigorously stirred overnight at room temperature. Subsequently, the mixture was dialyzed against Milli-Q water for 7 days, with the Milli-Q water changed twice a day. The purified solution was lyophilized, yielding the final HAMA product (yield of ca. 70%).

4.0.0.3. Ink Formulation: To prepare functional hydrogel inks for 3D-printed hydrogel bioelectronics, three distinct hydrogel inks were formulated, each designed for a specific structural layer of the device: a hydrogel-encapsulating layer (bottom layer), an adhesive layer (middle layer), and a conducting layer (top layer). The encapsulating layer ink consists of HAMA (5.0 *wt*%), PEGDA (1.0 *wt*%, M_w = 2000 Da), and α-KA (0.5 *wt*%); the adhesive layer ink is composed of PAHN (15.0 *wt*%), HAMA (5.0 *wt*%), PEGDA (1.0 *wt*%), and α-KA (0.5 *wt*%); and the conducting layer ink comprises PEDOT: PSS (6.0 *wt*%), MAG (3.0 *wt*%), PEGDGE (10.0 *wt*%, M_w = 400 Da), PEGDA (1.0 *wt*%), and α-KA (0.5 *wt*%). Each ink was thoroughly mixed at room temperature by magnetic stirring for 6 h, loaded into syringe barrels, and degassed (AR-100, Thinky) at 2000 rpm for 10 min to completely remove residual air bubbles. Finally, all hydrogel inks were stored at 4 °C until prior to 3D printing.

4.0.0.4. 3D Printing of Full Hydrogel Bioelectronics: The fabrication of 3D-printed hydrogel bioelectronics was performed using a 3D-Bioarchitect multi-nozzle workstation (Regenovo). The printing path was first designed using commercially available software, SolidWorks (Dassault Systmes), and then converted into G-code to control the x-y-z movements of the printing head. To ensure continuous and uniform printing paths, printability tests were conducted and the printing parameters, including the nozzle diameter, applied air pressure, and printing speed were optimized for each ink. The optimized printing parameters for each ink are as follows: conducting hydrogel ink was printed using a nozzle with a diameter of 0.16 mm at room temperature, with an air pressure of 0.3 MPa and a printing speed of 5 mm s^{-1}. Both bioadhesive and encapsulating hydrogel inks were printed using conical nozzles with a diameter of 0.16 mm, an air pressure of 0.1 MPa, and a printing speed of 15 mm s^{-1}. After 3D printing, the samples were placed in a UV curing chamber (CL-3000L) under a light intensity of 20 mW cm^{-2} for 3 min. Finally, the resulting 3D-printed hydrogel bioelectronics were dried at room temperature for 24 h and stored under −20 °C prior to further use.

4.0.0.5. Animal Tests: All animal experiments were performed in accordance with the guidelines approved by the Institutional Animal Care and Use Committee (IACUC). The experiments conducted at the Southern University of Science and Technology (SUSTech) were approved under the ethics approval number SUSTech-JY202403106. Additional experiments performed at Shuiyuntian *Co., LTD*. received approval from the company's IACUC under the ethics approval number SYT2024058.

4.0.0.6. In Vivo Vagus Nerve Stimulation: S.D. rats ≈200 g were anesthetized with 1–3% isoflurane in oxygen. After shaving the cervical region, an incision was made on the skin to expose the subcutaneous tissues. The cervical vagus nerve was carefully dissected. The 3D printed hydrogel bioelectronics were attached to the exposed vagus nerve, and the Au electrode was used as a control. The 3D-printed hydrogel bioelectronics were attached to the exposed vagus nerve. The integration between the hydrogel device and the back-end electronics was achieved by directly adhering the terminal region of the conductive hydrogel tracks to a commercial flexible printed circuit (FPC) cable. Biphasic charge-balanced rectangular voltage pulses (1 Hz, 0.01–0.5 V) were applied to stimulate the neural system. Vagus nerve and electrocardiogram signals were recorded using commercial electrodes (Taimeng Chengdu, BL420N) at a sampling frequency of 1 kHz and processed using *MATLAB* 2023b software.

4.0.0.7. Rat Stroke Model: Male S.D. rats (≈200 g) were anesthetized using isoflurane (2% oxygen) in an anesthetizing chamber. Anesthesia was maintained with a nose cone (1.5% oxygen), and the rats were secured in a stereotaxic apparatus (Shenzhen RWD Life Science *Co., Ltd.*). The midline of the scalp was disinfected with iodophor, and a midline incision was made to expose the skull. Three small holes were drilled at the following coordinates relative to the bregma: (1) AP (anterior-posterior) = −1.0 mm, ML (medial-lateral) = −2.5 mm, DV (dorsoventral) = −2.3 mm; (2) AP = +1.0 mm, ML = −2.5 mm, DV = −2.3 mm; (3) AP = +3.0 mm, ML = −2.5 mm, DV = −2.3 mm. ET-1, dissolved in ddH$_2$O, was injected into each hole at 2 µg per 2 µL. All the samples were prepared under sterile conditions and further sterilized under UV light for 3 h.

4.0.0.8. Statistical Analysis: All results are presented as the mean ± standard deviation (S.D.). All experiments were repeated at least three times, and each condition was analyzed in triplicate. One-way analysis of variance (one-way ANOVA) followed by Tukey's post-hoc test was used to evaluate statistical significance among multiple groups. A significance level of $p < 0.05$ was considered statistically significant. All statistical analyses were performed using Origin 8.0 (OriginLab, Northampton, MA, USA).

Supporting Information

Supporting Information is available from the Wiley Online Library or from the author.

Acknowledgements

The authors acknowledge the financial support by STI 2030-Major Projects (2022ZD0209500), National Natural Science Foundation of China (52373139 and U2436202), Guangdong Basic and Applied Basic Research Foundation (2024A1515240042), and Basic Research Program of Shenzhen (JCYJ20230807093419041, JCYJ20240813094159001 and 20231116101626002). The authors also gratefully acknowledge the support from the Shenzhen Science and Technology Innovation Commission (KJZD20240903101400001) and the Development and Reform Commission of Shenzhen Municipality (XMHT20240115003). The authors would also like to acknowledge the technical support from SUSTech Core Research Facilities.

Conflict of Interest

The authors declare no conflict of interest.

Data Availability Statement

The data that support the findings of this study are available from the corresponding author upon reasonable request.

Keywords

hydrogel bioelectronics, impedance matching, low-voltage stimulation, mechanical compliance, peripheral neuromodulation

Received: June 10, 2025
Revised: August 7, 2025

[1] T. Wyss-Coray, *Nature* **2016**, *539*, 180.
[2] T. Kim, H. J. Kim, W. Choi, Y. M. Lee, J. H. Pyo, J. Lee, J. Kim, J. Kim, J.-H. Kim, C. Kim, W. J. Kim, *Nat. Biomed. Eng.* **2023**, *7*, 149.
[3] K. Famm, B. Litt, K. J. Tracey, E. S. Boyden, M. Slaoui, *Nature* **2013**, *496*, 159.
[4] R. Feiner, T. Dvir, *Nat. Rev. Mater.* **2017**, *3*, 1.
[5] B. J. Woodington, J. Lei, A. Carnicer-Lombarte, A. Güemes-González, T. E. Naegele, S. Hilton, S. El-Hadwe, R. A. Trivedi, G. G. Malliaras, D. G. Barone, *Sci. Adv.* **2024**, *10*, eadl1230.
[6] Z. Shen, Q. Liang, Q. Chang, Y. Liu, Q. Zhang, *Adv. Mater.* **2024**, *36*, 2310365.
[7] Y. Xue, X. Chen, F. Wang, J. Lin, J. Liu, *Adv. Mater.* **2023**, *35*, 2304095.
[8] S. Choi, S. I. Han, D. Jung, H. J. Hwang, C. Lim, S. Bae, O. K. Park, C. M. Tschabrunn, M. Lee, S. Y. Bae, J. W. Yu, J. H. Ryu, S.-W. Lee, K. Park, P. M. Kang, W. B. Lee, R. Nezafat, T. Hyeon, D.-H. Kim, *Nat. Nanotechnol.* **2018**, *13*, 1048.
[9] T. Zhou, H. Yuk, F. Hu, J. Wu, F. Tian, H. Roh, Z. Shen, G. Gu, J. Xu, B. Lu, X. Zhao, *Nat. Mater.* **2023**, *22*, 895.
[10] Y. Liu, J. Li, S. Song, J. Kang, Y. Tsao, S. Chen, V. Mottini, K. McConnell, W. Xu, Y.-Q. Zheng, J. B.-H. Tok, P. M. George, Z. Bao, *Nat. Biotechnol.* **2020**, *38*, 1031.
[11] J. W. Salatino, K. A. Ludwig, T. D. Kozai, E. K. Purcell, *Nat. Biomed. Eng.* **2017**, *1*, 862.
[12] Y. Liu, J. Liu, S. Chen, T. Lei, Y. Kim, S. Niu, H. Wang, X. Wang, A. M. Foudeh, J. B.-H. Tok, Z. Bao, *Nat. Biomed. Eng.* **2019**, *3*, 58.
[13] X. Chen, Y. Feng, P. Zhang, Z. Ni, Y. Xue, J. Liu, *Adv. Mater.* **2025**, *37*, 2413476.
[14] K.-I. Song, H. Seo, D. Seong, S. Kim, K. J. Yu, Y.-C. Kim, J. Kim, S. J. Kwon, H.-S. Han, I. Youn, H. Lee, D. Son, *Nat. Commun.* **2020**, *11*, 4195.
[15] Y. Feng, L. Shan, Y. Wang, X. Chen, C. Wang, J. Liu, *ACS Nano* **2025**, *19*, 1667516684.
[16] W. G. Chung, J. Jang, G. Cui, S. Lee, H. Jeong, H. Kang, H. Seo, S. Kim, E. Kim, J. Lee, S. G. Lee, S. H. Byeon, J.-U. Park, *Nat. Nanotechnol.* **2024**, *19*, 688.
[17] J. A. Clancy, D. A. Mary, K. K. Witte, J. P. Greenwood, S. A. Deuchars, J. Deuchars, *Brain Stimul.* **2014**, *7*, 871.
[18] P. Zhang, Y. Yang, Z. Li, Y. Xue, F. Wang, L. Shan, Y. Wang, X. Shi, K. Wu, J. Liu, *Adv. Funct. Mater.* **2025**, 2422869.
[19] G. Hong, X. Yang, T. Zhou, C. M. Lieber, *Curr. Opin. Neurobiol.* **2018**, *50*, 33.
[20] H. Choi, Y. Kim, S. Kim, H. Jung, S. Lee, K. Kim, H.-S. Han, J. Y. Kim, M. Shin, D. Son, *Nat. Electron.* **2023**, *6*, 779.
[21] F. Wang, Y. Xue, X. Chen, P. Zhang, L. Shan, Q. Duan, J. Xing, Y. Lan, B. Lu, J. Liu, *Adv. Funct. Mater.* **2024**, *34*, 2314471.
[22] M. Yang, P. Chen, X. Qu, F. Zhang, S. Ning, L. Ma, K. Yang, Y. Su, J. Zang, W. Jiang, T. Yu, X. Dong, Z. Luo, *ACS Nano* **2023**, *17*, 885.
[23] Y. Zhang, N. Zheng, Y. Cao, F. Wang, P. Wang, Y. Ma, B. Lu, G. Hou, Z. Fang, Z. Liang, M. Yue, Y. Li, Y. Chen, J. Fu, J. Wu, T. Xie, X. Feng, *Sci. Adv.* **2019**, *5*, eaaw1066.
[24] Y. H. Cho, Y.-G. Park, S. Kim, J.-U. Park, *Adv. Mater.* **2021**, *33*, 2005805.
[25] M. J. Airaghi Leccardi, B. X. Desbiolles, A. Y. Haddad, B. C. Joy, C. Song, D. Sarkar, *Commun. Chem.* **2024**, *7*, 249.
[26] C. Dong, A. Carnicer-Lombarte, F. Bonafè, B. Huang, S. Middya, A. Jin, X. Tao, S. Han, M. Bance, D. G. Barone, B. Fraboni, G. G. Malliaras, *Nat. Mater.* **2024**, *23*, 969.
[27] R. Dong, L. Wang, Z. Li, J. Jiao, Y. Wu, Z. Feng, X. Wang, M. Chen, C. Cui, Y. Lu, X. Jiang, *ACS Nano* **2024**, *18*, 1702.

[28] Y. Cui, L. Li, C. Liu, Y. Wang, M. Sun, B. Jia, Z. Shen, X. Sheng, Y. Deng, *Nano Lett.* **2023**, *23*, 11693.
[29] N. Li, Y. Li, Z. Cheng, Y. Liu, Y. Dai, S. Kang, S. Li, N. Shan, S. Wai, A. Ziaja, Y. Wang, J. Strzalka, W. Liu, C. Zhang, X. Gu, J. A. Hubbell, B. Tian, S. Wang, *Science* **2023**, *381*, 686.
[30] G. Schiavone, S. P. Lacour, *Sci. Transl. Med.* **2019**, *11*, eaaw5858.
[31] S. Lee, Y. Inoue, D. Kim, A. Reuveny, K. Kuribara, T. Yokota, J. Reeder, M. Sekino, T. Sekitani, Y. Abe, T. Someya, *Nat. Commun.* **2014**, *5*, 5898.
[32] X. Chen, J. Zhang, G. Chen, Y. Xue, J. Zhang, X. Liang, I. M. Lei, J. Lin, B. B. Xu, J. Liu, *Adv. Funct. Mater.* **2022**, *32*, 2202285.
[33] Y. Xue, J. Zhang, X. Chen, J. Zhang, G. Chen, K. Zhang, J. Lin, C. Guo, J. Liu, *Adv. Funct. Mater.* **2021**, *31*, 2106446.
[34] H. Zhang, A. Mourran, M. Mller, *Nano Lett.* **2017**, *17*, 2010.
[35] S. Timoshenko, *J. Opt. Soc. Am.* **1925**, *11*, 233.
[36] S. Alben, B. Balakrisnan, E. Smela, *Nano Lett.* **2011**, *11*, 2280.
[37] W. M. Van Rees, E. Vouga, L. Mahadevan, *Proc. Natl. Acad. Sci. U. S. A* **2017**, *114*, 11597.
[38] R. Luo, J. Wu, N.-D. Dinh, C.-H. Chen, *Adv. Funct. Mater.* **2015**, *25*, 7272.
[39] D. Won, J. Kim, J. Choi, H. Kim, S. Han, I. Ha, J. Bang, K. K. Kim, Y. Lee, T.-S. Kim, J.-H. Park, C.-Y. Kim, S. H. Ko, *Sci. Adv.* **2022**, *8*, eabo3209.
[40] G. Li, K. Huang, J. Deng, M. Guo, M. Cai, Y. Zhang, C. F. Guo, *Adv. Mater.* **2022**, *34*, 2200261.
[41] Y. Wang, Z. Li, X. Chen, Y. Tan, F. Wang, Y. Du, Y. Zhang, Y. Su, F. Xu, C. Wang, W. Chen, J. Liu, *J. Mech. Phys. Solids* **2024**, *193*, 105867.
[42] K. Tybrandt, I. V. Zozoulenko, M. Berggren, *Sci. Adv.* **2017**, *3*, eaao3659.
[43] P. Chen, Q. Wang, X. Wan, M. Yang, C. Liu, C. Xu, B. Hu, J. Feng, Z. Luo, *Nano Energy* **2021**, *89*, 106327.
[44] E. M. Gordon, R. J. Chauvin, A. N. Van, A. Rajesh, A. Nielsen, D. J. Newbold, C. J. Lynch, N. A. Seider, S. R. Krimmel, K. M. Scheidter, J. Monk, R. L. Miller, A. Metoki, D. F. Montez, A. Zheng, I. Elbau, T. Madison, T. Nishino, M. J. Myers, S. Kaplan, C. B. D'Andrea, D. V. Demeter, M. Feigelis, J. S. B. Ramirez, T. Xu, D. M. Barch, C. D. Smyser, C. E. Rogers, J. Zimmermann, K. N. Botteron, et al., *Nature* **2023**, *617*, 351.
[45] M. Bönstrup, L. Krawinkel, R. Schulz, B. Cheng, J. Feldheim, G. Thomalla, L. G. Cohen, C. Gerloff, *Ann. Neurol.* **2019**, *86*, 853.
[46] E. C. Meyers, B. R. Solorzano, J. James, P. D. Ganzer, E. S. Lai, R. L. Rennaker, M. P. Kilgard, S. A. Hays, *Stroke* **2018**, *49*, 710.
[47] Z. Sun, W. Baker, T. Hiraki, J. H. Greenberg, *Brain Stimul.* **2012**, *5*, 1.
[48] I. Ay, R. Nasser, B. Simon, H. Ay, *Brain Stimul.* **2016**, *9*, 166.
[49] Y. Lampl, G. Fleminger, R. Gilad, R. Galron, I. Sarova-Pinhas, M. Sokolovsky, *Stroke* **1997**, *28*, 1951.
[50] A. Alrafiah, E. Alofi, Y. Almohaya, A. Hamami, T. Qadah, S. Almaghrabi, N. Hakami, M. S. Alrawaili, H. O. Tayeb, *J. Inflamm. Res.* **2021**, *14*, 4893.